Inorganic Chemistry

Article

pubs.acs.org/IC

Effect of Carbon Coating on the Physicochemical and Electrochemical Properties of Fe_2O_3 Nanoparticles for Anode Application in High Performance Lithium Ion Batteries

A. Iturrondobeitia,[†,‡] A. Goñi,[†,§] I. Orue,[∥] I. Gil de Muro,[†,§] L. Lezama,[†,§] M. M. Doeff,[⊥] and T. Rojo*[,†,‡]

[†]Departamento de Química Inorgánica, Universidad del País Vasco UPV/EHU, P.O. Box 644, 48080 Bilbao, Spain

[‡]Parque Tecnológico de Álava, CIC energiGUNE, Albert Einstein 48, 01510 Miñano, Álava, Spain

[§]Parque Científico y Tecnológico de Bizkaia, BCMATERIALS, Ibaizabal Bidea 500, 48160 Derio, Spain

[∥]Departamento de Electricidad y Electrónica, Facultad de Ciencia y Tecnología, Universidad del País Vasco (UPV-EHU), P.O. Box 644, 48080, Bilbao, Spain

[⊥]Environmental Energy Technologies Division, Lawrence Berkeley National Laboratory, 1 Cyclotron Road MS62R0203, Berkeley, California 94720-8168, United States

ABSTRACT: Nanoparticulate Fe_2O_3 and Fe_2O_3/C composites with different carbon proportions have been prepared for anode application in lithium ion batteries (LIBs). Morphological studies revealed that particles of Fe_2O_3 in the composites were well-dispersed in the matrix of amorphous carbon. The properties of the γ-Fe_2O_3 nanoparticles and the correlation with the particle size and connectivity were studied by electron paramagnetic resonance, magnetic, and Mössbauer measurements. The electrochemical study revealed that composites with carbon have promising electrochemical performances. These samples yielded specific discharge capacities of 1200 mAh/g after operating for 100 cycles at 1C. These excellent results could be explained by the homogeneity of particle size and structure as well as the uniform distribution of γ-Fe_2O_3 nanoparticles in the *in situ* generated amorphous carbon matrix.

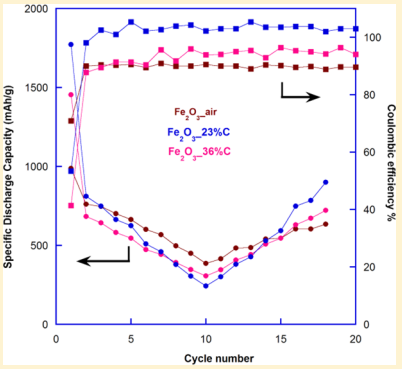

INTRODUCTION

As one of the most important and widely used rechargeable power sources, lithium ion batteries (LIBs) have attracted extensive attention, due to their excellent performance in portable electronics, electric vehicles (EVs), and hybrid electric vehicles (HEVs).[1−4] For commercial LIBs, graphite is the most widely used anode material because of its low cost, high abundance, and outstanding electrochemical performance. However, the theoretical capacity is only 372 mAh/g. To develop higher energy density systems, denser and higher capacity anode materials are needed. For this reason, 3d transition metal oxides (MO_x) are among one of the most promising next-generation anode materials under consideration.[5,6] Contrary to conventional intercalation or alloying mechanisms, the high Li^+ storage capacity is derived from conversion reactions as shown below:[7]

$$M_xO_y + 2yLi^+ + 2ye^- \rightarrow xM + yLi_2O$$

The transition metal oxides are ultimately reduced to the elements leading to composite materials consisting of metallic nanoparticles dispersed in an amorphous Li_2O matrix. The large irreversible capacity that these materials suffer in the first cycle is a major obstacle for potential applications of most conversion anodes. This way, in full lithium ion cells, the extra cathode material consumed as irreversible capacity would lead to a decrease in energy density and to an increase in the cost. However, the large irreversible capacity can be successfully address by surface prelithiation treatments or by thin film nanostructuration.[8,9]

Among the choices of metal oxides, Fe_2O_3 (iron oxide) has been regarded as a very appealing candidate because of its high theoretical capacity (1007 mAh/g), nontoxicity, high corrosion resistance, and low materials and processing costs.[10] However, further optimization of iron oxides as anode materials is needed due to their poor cycling performance and limited rate capability. Many attempts have been made to improve the reversible capacity, cycling stability, and rate capability of Fe_2O_3. Toward this end, introducing carbonaceous materials, such as graphene,[11,12] carbon nanotubes,[13] or carbon fibers,[14] improves the cycling stability and rate capability of iron oxides.

Carbonaceous materials, as well as increasing the electronic contact between the iron oxide particles, also buffer the volume and structural changes associated with the transformation of iron oxide particles into metallic iron during the discharge/charge process. Nevertheless, most of the preparation methods of high performance iron oxides are extremely complicated and are of low yield. Therefore, a facile synthesis method for large-

Received: January 27, 2015
Published: May 18, 2015

DOI: 10.1021/acs.inorgchem.5b00203
Inorg. Chem. 2015, 54, 5239−5248

scale production of iron oxides for anode materials of LIBs is required. Here, a freeze-drying synthesis procedure has been employed, which, as well as being a cheap and easy method, can be easily implemented as part of an industrial process. Moreover, this synthesis method presents other advantages such as homogeneity of reactants, the possibility of introducing a carbon source, and the ability to use lower calcination temperatures.[15] This synthesis method has already been proven in our group to be useful to obtain nanosized cathodic materials with exceptional electrochemical performance.[16]

In this study, three different composites based on nanosized Fe_2O_3 and carbon were successfully synthesized by the freeze-drying method. We report on the structural, morphologic, magnetic, spectroscopic, and electrochemical characterization of the synthesized samples, establishing correlations among the composition, morphology, and electrochemical performance.

RESULTS AND DISCUSSION

The amount of carbon in the samples was determined by elemental analysis. Table 1 summarizes the percentage of C in each sample. Accordingly, the samples were called Fe_2O_3_23% C, Fe_2O_3_36%C, and Fe_2O_3_air (because this material was calcined in air).

Table 1. Percentage of Carbon in Each Sample

sample	Fe_2O_3_air	Fe_2O_3_23%C	Fe_2O_3_36%C
% C	0	23.2 (8)	35.9 (5)

Figure 1 shows the XRD patterns of Fe_2O_3_air and the two composites. For the Fe_2O_3_air sample, most of the major diffraction peaks could be indexed to hematite, α-Fe_2O_3 (Powder Diffraction File 89-0599 PDF card). Some weak reflections corresponding to the maghemite polymorph, γ-Fe_2O_3, were also detected (Powder Diffraction File 89-0599 PDF card). The XRD patterns of Fe_2O_3_23%C and Fe_2O_3_36%C composites were very similar, and all of the diffraction peaks could be indexed to maghemite γ-Fe_2O_3. The theoretical and experimental cell parameters obtained from profile fittings are shown in Table 2.

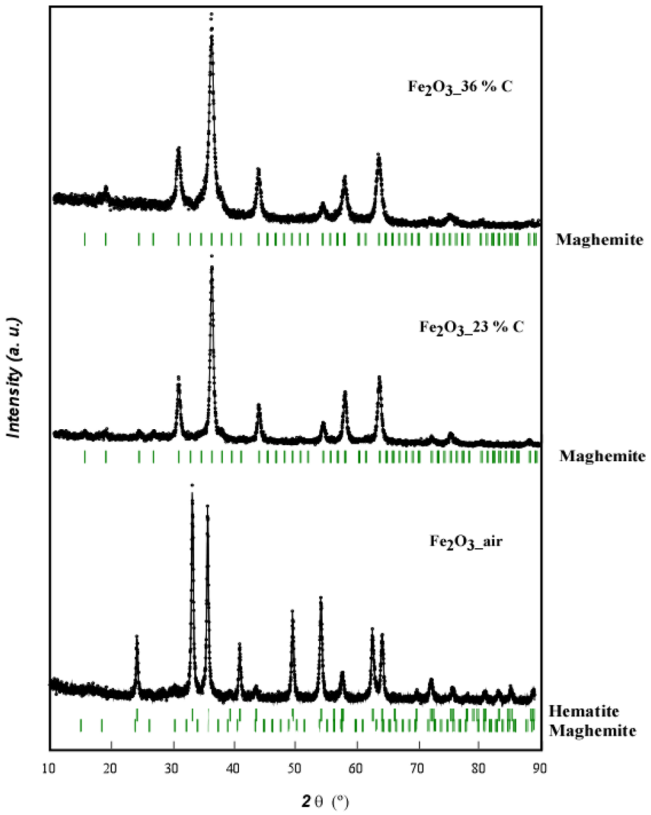

Figure 1. XRD patterns of Fe_2O_3_air, Fe_2O_3_23%C, and Fe_2O_3_36% C.

Table 2. Theoretical and Experimental Cell Parameters for All the Compounds

cell param (Å)	Fe_2O_3_air	Fe_2O_3_23%C	Fe_2O_3_36%C
	Experimental		
a	5.0346 (4)	8.3531 (9)	8.3643 (1)
b	5.0346 (4)		
c	13.7519 (2)		
	Theoretical		
a	5.032[a]	8.351[b]	
b	5.032		
c	13.733		
	Space Group		
	$R\bar{3}c$	$P4132$	
	Compound		
	α-Fe_2O_3	γ-Fe_2O_3	

[a]Powder Diffraction File 89-0599 PDF card (R3P7). [b]Powder Diffraction File 39-1346 PDF card (R3P7).

The average size of particles for Fe_2O_3_23%C and Fe_2O_3_36%C composites was determined from the full width at half-maximum (fwhm) of the X-ray diffraction peak using Scherrer's equation shown below:[17]

$$D = \frac{K\lambda}{B_{\text{estruc}} \cos\theta}$$

Here D is the particle diameter, λ the X-ray wavelength, B the fwhm of a diffraction peak, (311) in our case, θ the diffraction angle, and K is the Scherrer's constant of the order of unit for usual crystals.[18] The calculated size of our specimens from the deconvolution of (311) diffraction maxima was 15 and 12 nm for Fe_2O_3_23%C and Fe_2O_3_36%C, respectively. The nanometric particle size could be attributed to the favorable conditions that these syntheses have to form nanoparticles as the carbon source acts preventing the growth of particle size. In this context, since is very strange to find α polymorph nanoparticles, γ polymorph nanoparticles were formed, which is the second most stable polymorph of Fe_2O_3.

This calculation was not carried out for the Fe_2O_3_air sample since, as has been mentioned before, this sample contains an impurity of γ-Fe_2O_3. This way, there are no diffraction maxima corresponding to the α-Fe_2O_3 polymorph that are not affected by the contribution of the diffraction maxima of the impurity phase.

Figure 2a–c shows transmission electron micrographs of the Fe_2O_3_air, Fe_2O_3_23%C, and Fe_2O_3_36%C samples, respectively. The Fe_2O_3_air sample is heterogeneous, made up of irregularly shaped particles with a wide range of sizes (7–100 nm). The micrograph of the Fe_2O_3_23%C sample, Figure 2b, shows that it consists of nanometric size particles ranging in diameter from 10 to 20 nm, covered by a carbonaceous web. The Fe_2O_3_36%C composite, Figure 2c, is made up of 10 nm homogeneous spherical nanoparticles embedded in the *in situ*

DOI: 10.1021/acs.inorgchem.5b00203
Inorg. Chem. 2015, 54, 5239–5248

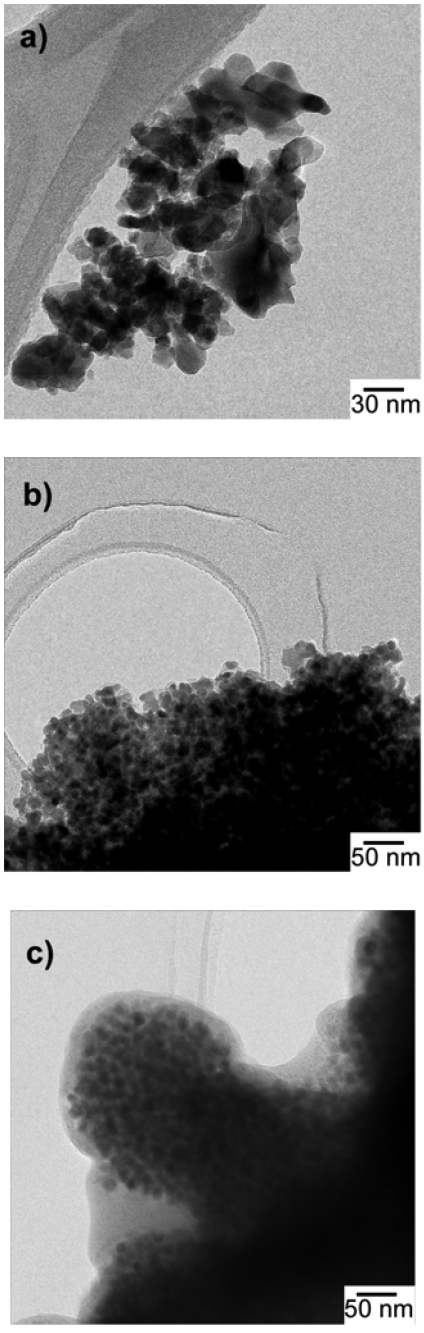

Figure 2. TEM images of (a) Fe_2O_3_air, (b) Fe_2O_3_23%C, and (c) Fe_2O_3_36%C.

generated carbon matrix. The particle size of γ-Fe_2O_3 in the Fe_2O_3_36%C sample was the smallest of all the samples, because the high amount of carbon in this composite prevented their growth.

The EPR spectra of the samples were recorded at X-band at room temperature (Figure 3). A similar pattern was observed in the three cases: a very broad signal centered at a Landé factor g close to 2.18−2.20. This signal is characteristic of ferri/ferromagnetic systems.[19] However, the EPR signal of the Fe_2O_3_air sample is made up of two contributions. The first is the widest and is centered at a Landé factor g = 2. This contribution can be attributed to the antiferromagnetic oxide α-Fe_2O_3, which is the main component of Fe_2O_3_air. The second,

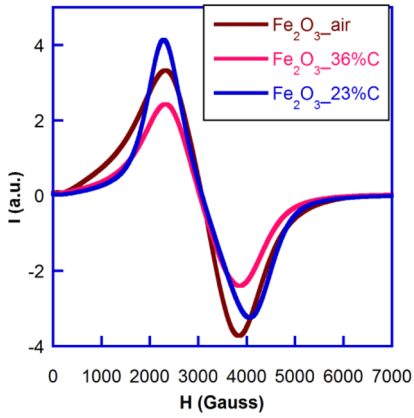

Figure 3. EPR spectra of Fe_2O_3_air, Fe_2O_3_23%C, and Fe_2O_3_36%C samples.

narrower contribution is centered at a Landé factor g = 2.18 and can be assigned to the γ-Fe_2O_3 oxide impurity.

A comparison of the Fe_2O_3_23%C and Fe_2O_3_36%C EPR patterns shows that the composite with the higher amount of carbon has a more isotropic signal, probably due to the smaller Fe_2O_3 particle size. The isotropic character of the EPR signal can be explained as due to the orientation of the spins of the very small particles under the influence of an applied external magnetic field (see ref 19).

Figure 4 shows the magnetic hysteresis loops at 5 K and room temperature of the Fe_2O_3_air sample in the plots of magnetization versus the applied magnetic field. The magnetic response to the external field matches the expected ferrimagnetic behavior due to the presence of the γ-Fe_2O_3 secondary phase. The magnetization is close to saturation under relatively small applied fields (<5 kOe). However, there are also quasilinear contributions to magnetization that are almost independent of temperature, which are visible in the slope of the hysteresis loops at high fields. This feature is compatible with the presence of an antiferromagnetic phase of high ordering temperature as it is α-Fe_2O_3, which is the main compound of this sample as detected in the XRD diffraction patterns.

After subtraction of a linear dependence from the $M(H)$ curves at 5 K, it is straightforward to estimate the percentage of γ-Fe_2O_3 by assuming a saturation magnetization value of 85 emu/g,[20] corresponding to pure maghemite. This simple calculation yields a relative content for the ferrimagnetic phase of at least 13% in weight. With the consideration that saturation magnetization is underestimated it could be better determined by other techniques such as Mössbauer spectroscopy. It could also be expected to determine the concentration of the two phases from the XRD data. However, in the present case the XRD patterns are affected by nanosizing, and thus, it is difficult to determine the relative volume percentage of each phase due to peak broadening.

The precise details of the loop at room temperature (Figure 4b) show a small but significant hysteresis with a coercive field of 31 Oe, indicating that at room temperature this sample is below the thermal activation threshold to the superparamagnetic state. At low temperatures (5 K) the coercive field is 410 Oe. Additionally, the hysteresis loop is not perfectly centered, but slightly shifted to negative fields by around 25 Oe, which shows little dependence on the external field applied during the cooling from room temperature. Both phenomena, the

DOI: 10.1021/acs.inorgchem.5b00203
Inorg. Chem. 2015, 54, 5239−5248

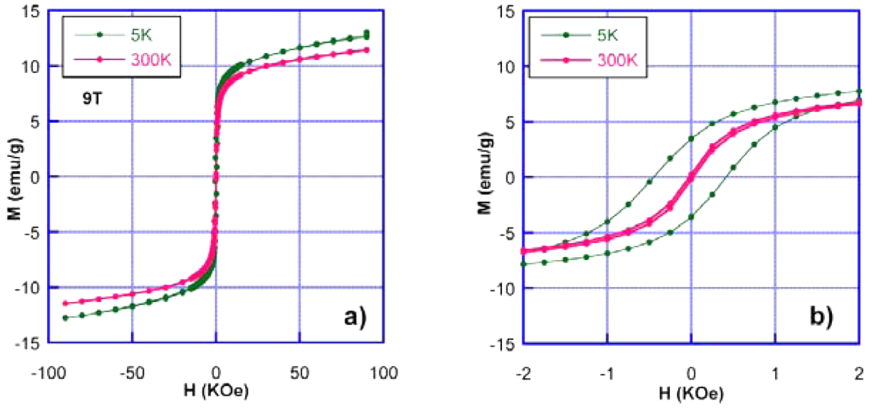

Figure 4. Hysteresis loops at 5 K and room temperature of the Fe_2O_3_air sample.

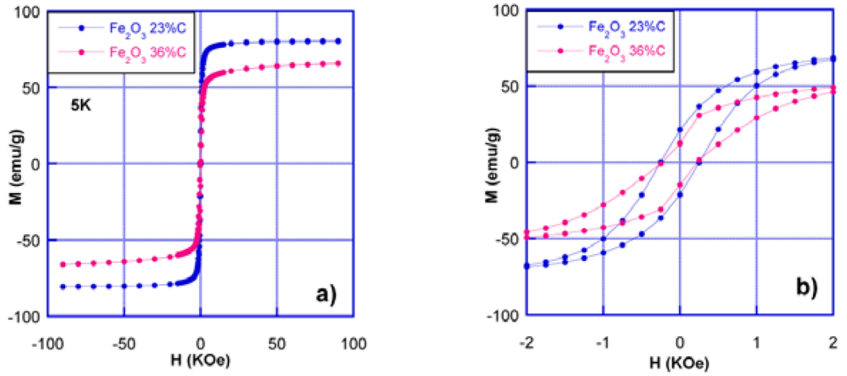

Figure 5. Hysteresis loops performed in samples Fe_2O_3_23%C and Fe_2O_3_36%C at 5 K.

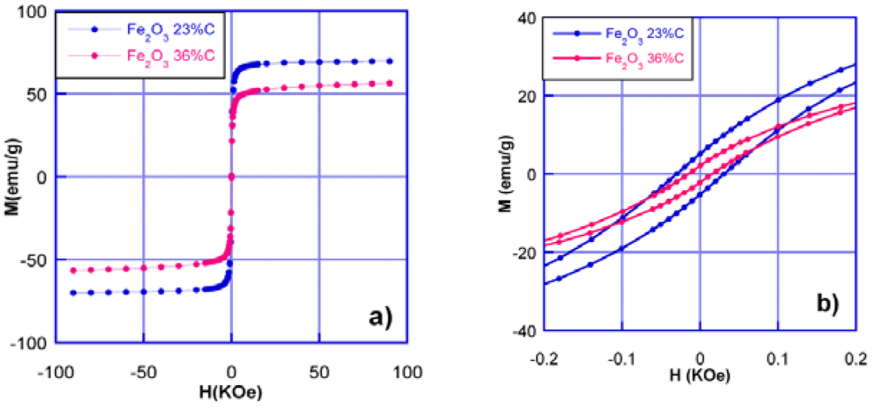

Figure 6. Room temperature magnetization measurements for Fe_2O_3_23%C and Fe_2O_3_36%C.

magnetic hardening and the small exchange bias, are probably related to the interfaces between α-Fe_2O_3 and γ-Fe_2O_3 phases.

Figure 5a,b shows the hysteresis loops obtained on samples Fe_2O_3_23%C and Fe_2O_3_36%C at 5 K. Unlike the previous case, the magnetic behavior is expected to be entirely related to the maghemite phases. In fact, the magnetization of Fe_2O_3_23%C perfectly saturates at 80 emu/g, which is very close to the value of pure maghemite in bulk. In contrast, Fe_2O_3_36%C becomes harder to saturate, and maximum magnetization lies clearly below Fe_2O_3_23%C, at around 63 emu/g. In both samples the coercive field is very similar (~250 Oe) and smaller than in Fe_2O_3_air, in agreement with values reported in the literature for maghemite nanoparticles of similar sizes.[21] The low field region displayed in Figure 5b shows, however, some differences: the central narrowing of the magnetization versus field in Fe_2O_3_36%C suggests the existence of two magnetic contributions. This feature, together with the lack of saturation at high fields can be explained as originating from very small superparamagnetic particles, whose magnetization does not saturate at 5 K and consequently also reduces the average magnetization of the sample.

As shown in Figure 6b the room temperature magnetization measurements indicate that the magnetic hysteresis is higher for the Fe_2O_3_23%C sample (30 Oe) than for Fe_2O_3_36%C (20 Oe). These samples are still in the ferromagnetic regime at room temperature, and the values of coercive fields are consistent with particle sizes deduced from TEM. In magnetic single domains the coherent magnetization reversal occurs at

DOI: 10.1021/acs.inorgchem.5b00203
Inorg. Chem. 2015, 54, 5239−5248

higher fields for larger particles.[22] This is exactly what is observed in Fe_2O_3_23%C, which has particles averaging 15 nm in size, compared to the Fe_2O_3_36%C sample, which is composed of 10 nm average size particles. For isolated maghemite nanoparticles of these sizes, the transition to the superparamagnetic state in dc magnetic measurements is expected to lie below room temperature. The existence of a significant percentage of ferromagnetic particles in these samples reflects the high degree of agglomeration observed in TEM.

The measurement of the high field magnetization as a function of temperature, shown in Figure 7, highlights the small

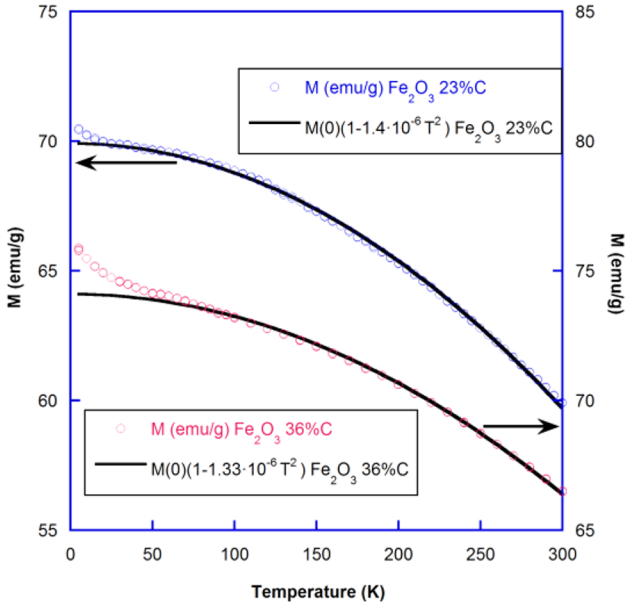

Figure 7. Measurements of the high field magnetization as a function of temperature for Fe_2O_3_23%C and Fe_2O_3_36%C samples.

but significant differences between Fe_2O_3_23%C and Fe_2O_3_36%C. As long as the applied constant field is high enough to overcome the anisotropy field and the effect of thermal fluctuations, this experiment directly supplies the saturation magnetization of the sample. The first requirement can be easily observed in these samples only by using a field much higher than the anisotropy fields, which are around 0.5 kOe. Therefore, the curves of Figure 7 indicate that at 90 kOe the magnetization is not completely saturated since a nearly paramagnetic contribution is the origin of a small tail at low temperatures. This effect, which is much stronger for Fe_2O_3_36%C, could be attributed to the existence of very small and isolated magnetic nanoparticles, whose blocking temperatures are very close to or below 5 K.

The high field magnetization decreases with temperature as T^2, as shown in Figure 7. This exponent, clearly departing from the standard $T^{3/2}$ characteristic of the spin-wave excitation model, has been found in other nanoparticle systems and explained as a consequence of the finite size effects. The proportionality factor (B) in the equation $M(T) = M(0)(1 - BT^2)$, used to fit the data, is quite similar in the Fe_2O_3_23%C and Fe_2O_3_36%C composites $(1.4 \text{ and } 1.33 \times 10^{-6}\ K^{-2})$ and is in good agreement with previously reported data.[23]

Room temperature Mössbauer spectra of samples Fe_2O_3_air, Fe_2O_3_23%C, and Fe_2O_3_36%C are presented in Figures 8 and 9. In all three cases the contribution from sextets corresponding to hyperfine fields close to 50 T is observed, characteristic of iron oxides with magnetic ordering. Additionally, it should be considered that the apparent line-width of these spectra is significantly larger than the natural one. This broadening is rather predictable for nanoparticle materials in measurements performed at room temperature because of the existence of thermal activation phenomena as well as a certain degree of structural disorder.[24,25] For simplicity, the theoretical model has been built with a maximum of 4 subspectra with variable line widths.

The spectrum of Fe_2O_3_air exhibits a major sextet at 51.5 T with little broadening. Additionally, two other minor contributions corresponding to smaller hyperfine fields of around 48.7 and 44.2 T can be observed. As can be deduced from Figure 8, the three spectra are arranged symmetrically, with isomer shifts lower than 0.4 mm/s and very small quadrupolar splittings. On the basis of this, the existence of Fe^{2+} ions can be discarded. The hyperfine parameters of the

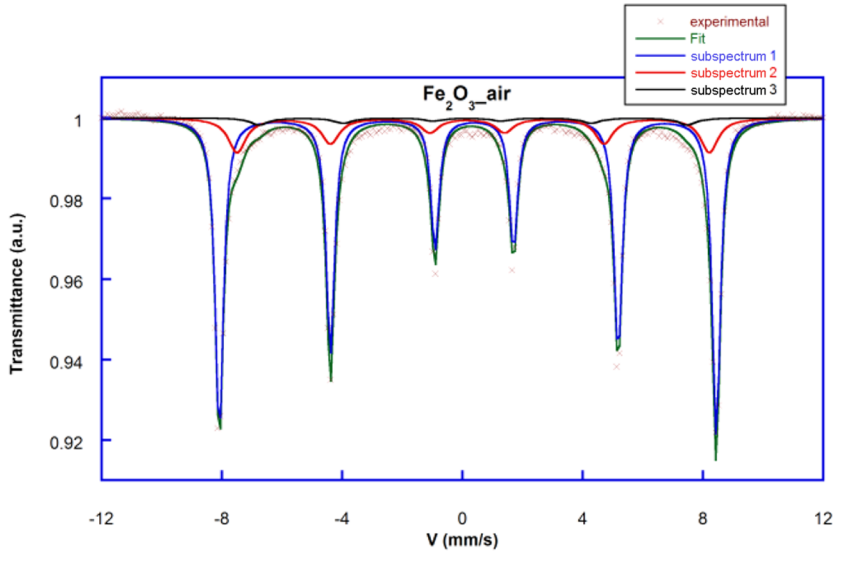

Figure 8. Mössbauer spectra of sample Fe_2O_3_air.

DOI: 10.1021/acs.inorgchem.5b00203
Inorg. Chem. 2015, 54, 5239−5248

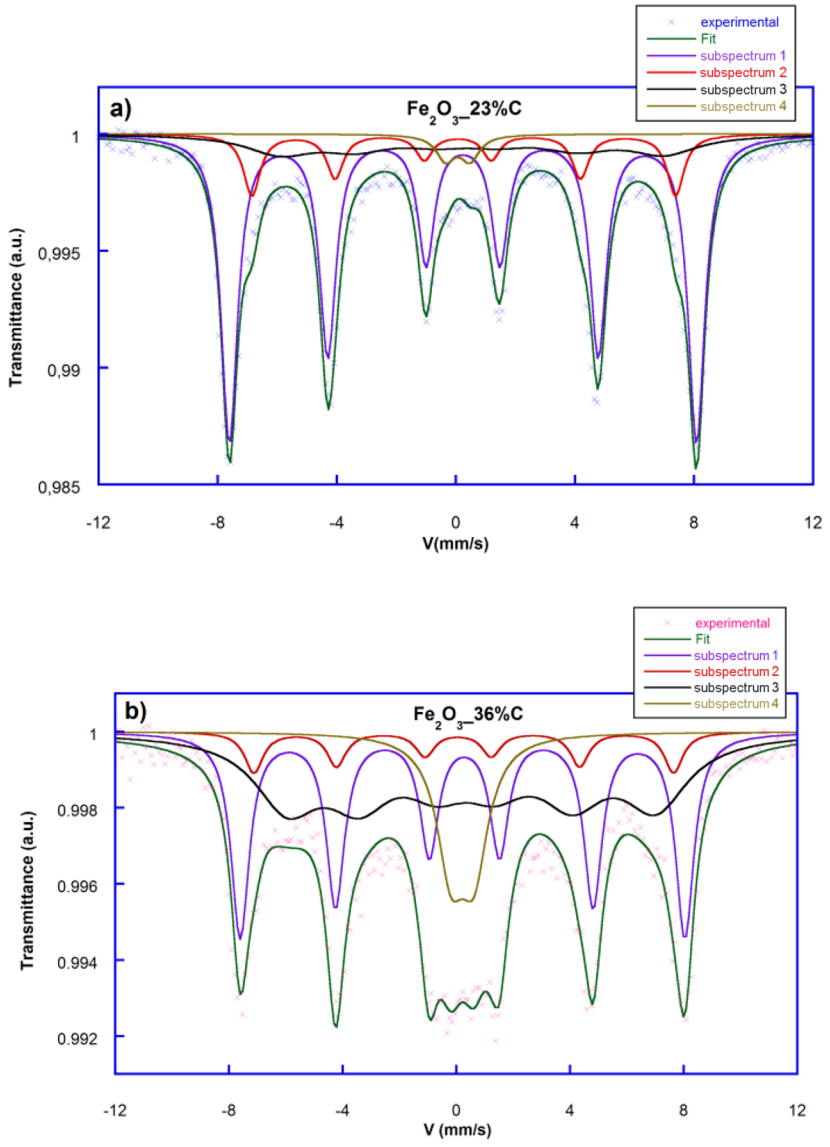

Figure 9. Mössbauer spectra of samples (a) Fe_2O_3_23%C and (b) Fe_2O_3_36%C.

main sextet are in good agreement with the data reported in the literature for α-Fe_2O_3.[26]

The other two minor sextets located at 48.7 and 44.2 T should correspond to the ferrimagnetic contribution observed in the hysteresis loops of Fe_2O_3_air in Figure 4. The X-ray diffraction pattern of this sample indicates the existence of a small percentage of γ-Fe_2O_3, which could explain this ferrimagnetic contribution. It is well-known that the Mössbauer spectrum of pure maghemite in the bulk state is composed of two sextets with almost identical hyperfine fields of 50.4 and 50.6 T in the approximate ratio of 1:1.67.[27] Thus, it could be said that the two minor sextets of sample Fe_2O_3_air do not correspond to different crystallographic positions of Fe^{3+} in the maghemite structure. However, similar results have been reported in samples composed of maghemite nanoparticles.[28] This decrease in the hyperfine field value is usually explained as an effect driven by the thermal fluctuations of the atomic magnetic moments in the vicinity, due to the transition to a superparamagnetic state. These fluctuations are strongly dependent on the total anisotropy energy of the nanoparticle (KV). Therefore, in multimodal size populations, different subspectra arise as well as different effective magnetic anisotropies. In this particular case, the second effect seems to be the most likely reason for the two minor magnetic contributions. These data are in good agreement with those observed in the transmission electron microscopy images where the existence of large agglomerates together with isolated particles were observed. On the basis of this, the isolated particles can be assigned to the smaller hyperfine field component of 44.2 T.

The determination of the relative contents of α-Fe_2O_3 and γ-Fe_2O_3 phases in the Fe_2O_3_air sample can be determined by computing the total resonant area of the minor subspectra to that of the total. This gives an estimated value of 21% of Fe belonging to the γ phase.

The Mössbauer spectra of Fe_2O_3_23%C and Fe_2O_3_36%C samples, (Figure 9), differ in some important aspects from that of Fe_2O_3_air. The width of the resonant lines became larger, and consequently, the subspectra are less resolved. This is related to the smaller average particle sizes of Fe_2O_3_23%C and Fe_2O_3_36%C compared to that of Fe_2O_3_air. The quantitative analysis of these spectra needs at least four sextets to fit the

DOI: 10.1021/acs.inorgchem.5b00203
Inorg. Chem. 2015, 54, 5239−5248

Table 3. Mössbauer Spectra Parameters for Fe_2O_3_air, Fe_2O_3_23%C, and Fe_2O_3_36%C Samples

	Fe_2O_3_air			Fe_2O_3_23%C				Fe_2O_3_36%C			
subspectra	1	2	3	1	2	3	4	1	2	3	4
IS (mm/s)	0.3	0.3	0.3	0.3	0.16	0.3	0.3	0.3	0.16	0.3	0.3
QS (mm/s)	0.3	0.2	0.2	0.3	0.2	0.2	0.8	0.3	0.2	0.2	0.8
W (mm/s)	0.3	0.7	0.7	0.8	0.8	2.7	1.2	0.8	0.8	1.8	1.2
B_{HF} (T)	51.2	48.7	44.2	48.7	44.2	40		48.7	45.4	39	
% Fe	78.2(4)	18.2(3)	3.6(1)	67.6(9)	13.5(1)	16(1)	2.9(3)	37(1)	7.3(1)	42(3)	13.8(3)

experimental data accurately. Values of the corresponding hyperfine parameters are presented in Table 3. The main sextet has a hyperfine field of approximately 48.7 T in both samples, very similar to that found in sample Fe_2O_3_air for the second contribution, which has been assigned to strongly agglomerated maghemite nanoparticles. Although the large broadening of the resonant lines (w = 0.8 mm/s) leads to much uncertainty in the isomer shift and quadrupole splitting of this contribution, the values are compatible with those expected for Fe^{3+}.

The wide doublet (subspectra 4 in Table 3) appearing in both samples originates from nanoparticles whose relaxation time is much smaller than the window time of the Mössbauer effect ($\sim 10^{-8}$ s). This phenomenon is much more apparent in Fe_2O_3_36%C (13%) than in Fe_2O_3_23%C (3%), which is in good agreement with the magnetization measurements. The existence of nanoparticles with particle sizes smaller than 4 nm explains the lack of saturation at high fields in the low temperature region (below 10 K) clearly observed for the Fe_2O_3_36%C composite.[29] Despite the large uncertainty produced by the line broadening, both the isomer shift and the quadrupole splitting are the same for Fe_2O_3_23%C and Fe_2O_3_36%C composites.

Finally, the two intermediate sextets (subspectra 2 and 3) correspond to roughly the same hyperfine fields, 44 and 40 T, in both compounds. The ratio of the contribution at 44 T, which is also present in sample Fe_2O_3_air, to the main one (48.7 T) is exactly the same in the three cases (1:4). This indicates the existence of high purity well-defined maghemite nanoparticles, whose concentration is maximum for the sample Fe_2O_3_23%C (%13.5). The low hyperfine field contribution at around 40 T (subspectra 3) becomes much more abundant in sample Fe_2O_3_36%C, as it is composed of smaller nanoparticles. The reduction in size could increase the thermal fluctuation of the spins in this sample.

To evaluate the electrochemical performance, lithium half-cells containing Fe_2O_3_air and Fe_2O_3_23%C and Fe_2O_3_36%C composite materials were discharged at current densities corresponding to C/10 and 1C rates. Figure 10a–c shows the discharge–charge curves of Fe_2O_3_air, Fe_2O_3_23%C, and Fe_2O_3_36%C, respectively, at C/10. All of these curves exhibit similar profiles. The first two regions located at 1.6 and 1.1 V can be attributed to the insertion of Li^+ in Fe_2O_3.[30] The third region situated at 0.8 V corresponds to the structural destruction of the iron oxide to ultimately give metallic iron, Fe^0.

The theoretical capacity of Fe_2O_3 for complete reduction of Fe^{3+} to Fe^0 is 1007 mAh/g, corresponding to a maximum lithium uptake of 6 Li^+ per Fe_2O_3 formula unit. However, Fe_2O_3_air, Fe_2O_3_23%C, and Fe_2O_3_36%C samples have delivered initial discharge specific capacities of 1216, 1451, and 1567 mAh/g, which are much larger than the theoretical capacity. This extra capacity is located in the gradually sloping low voltage region (region 4), and can be ascribed in part to the

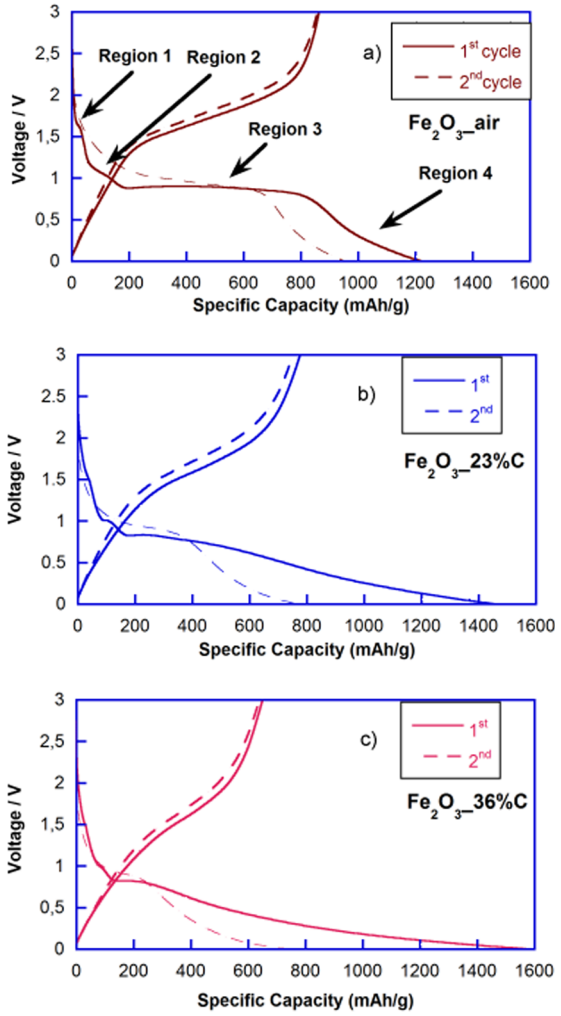

Figure 10. Discharge–charge curves of Fe_2O_3_air, Fe_2O_3_23%C, and Fe_2O_3_36%C, at C/10.

decomposition of the electrolyte to form a solid–electrolyte interphase (SEI).[31,32] In addition, electrochemical processes involving carbon may also contribute extra capacity, as this material is active at low voltage. Additionally, some authors have also reported possible pseudocapacitive contributions to overall electrode capacity.[33−35] The Fe_2O_3_23%C and Fe_2O_3_36%C samples contain 23% and 36% of *in situ* generated carbon, respectively, in addition to the 15% of Super P carbon added to the composite electrode. The length of the final slope shows that the capacity provided by external factors is larger for Fe_2O_3_36%C than for Fe_2O_3_air and Fe_2O_3_23%C, most likely indicating that the *in situ* carbon was electroactive during the first discharges. In this context, enhanced capacities have also been observed in the literature for graphene composites, such as graphene-wrapped Fe_3O_4 and

DOI: 10.1021/acs.inorgchem.5b00203
Inorg. Chem. 2015, 54, 5239–5248

graphene/amorphous iron oxyhydroxide composites among others.[36,37]

The cycling stability of the electrodes based on Fe_2O_3_air, Fe_2O_3_23%C, and Fe_2O_3_36%C was investigated at a current rate of 1C. As shown in Figure 11, capacity retention was better

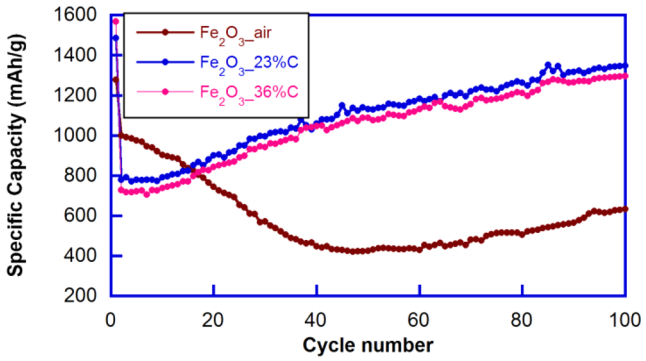

Figure 11. Cyclability of Fe_2O_3_air, Fe_2O_3_23%C, and Fe_2O_3_36%C samples at 1C rate.

for the carbon composites compared to that of Fe_2O_3_air. This fact could be attributed to the heterogeneity of the Fe_2O_3_air sample as well as to the lack of an *in situ* generated carbon matrix in this compound, which improved connectivity in the other samples. The heterogeneity of the Fe_2O_3 sample may have resulted in inactivation of some Li_2O/Fe regions after discharge due to disconnection. The carbon matrix enhances the cycling performance of the samples since it is electroactive at low voltages which improves the electrical connection between the nanoparticles and facilitates the accommodation of the structure change associated with successive charge and discharge cycles. In addition, an increase of the capacity values during cycling was evident for all the compounds, for Fe_2O_3_23%C and Fe_2O_3_36%C composites from the first cycles and for Fe_2O_3_air from the 60th cycle on. This fact could be ascribed to the formation of a polymeric gel that can be several nanometers thick.[38] The gel appears to contain poly(ethylene oxide) (PEO) oligomers whose formation is initiated by the reduction of the dimethyl carbonate (DMC) and ethylene carbonate (EC), electrolyte solvents, to lithium alkoxides and alkylcarbonates. This polymeric gel coats the particles, possibly contributing to the preservation of their integrity and accumulating additional lithium on its surface, thereby contributing to an extra capacity.[39] Moreover, the specific discharge capacities obtained for the cells containing the Fe_2O_3_23%C and Fe_2O_3_36%C composites exceed the theoretical capacity, which could be ascribed, in part, to two reasons. The first one is the enhanced decomposition of the electrolyte to form the SEI. In this sense, it would not be unreasonable to suspect that during the later cycles the SEI is disrupted due to morphological changes, exposure of fresh surfaces, or changes in the redox processes of the iron oxide. This way, the reformation of SEI is required adding extra capacity to the later cycles. The second reason is the electrochemical activity of the *in situ* generated carbon matrix.

In order to investigate the extra capacity provided by carbon, the 80th charge/discharge curves for Fe_2O_3_air and Fe_2O_3_36%C (representative also for Fe_2O_3_23%C since both composites show a very similar behavior) are shown in Figure 12 as an example. From here, it can be deduced that the extra capacity provided under 0.5 V is much larger for the

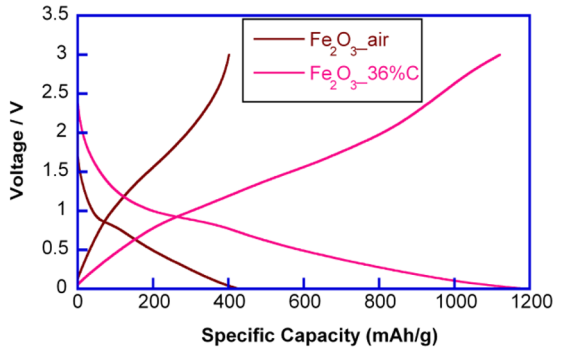

Figure 12. 80th charge/discharge curves for Fe_2O_3_air and Fe_2O_3_36%C samples.

composites than for Fe_2O_3. Moreover, it can be concluded that the polarization of composite materials is lower than that of Fe_2O_3. Similar results have been reported in the literature for Fe_2O_3 carbonaceous composites made up of nanometric particles.[40]

Figure 13 shows the Coulombic efficiencies at C/10 (defined as the ratio between charge and discharge capacity) of the cells

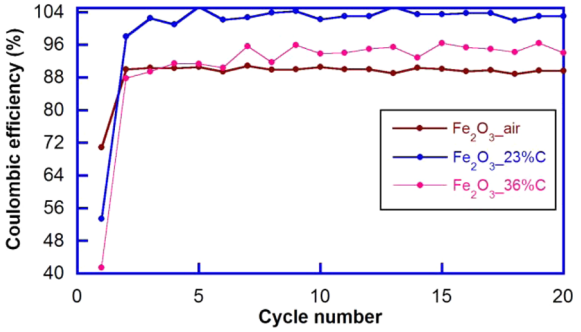

Figure 13. Coulombic efficiencies for Fe_2O_3_air, Fe_2O_3_23%C, and Fe_2O_3_36%C samples.

containing the three types of samples for the first 20 cycles. The Coulombic efficiencies in the first cycles were only 70%, 53%, and 41% for the Fe_2O_3_air, Fe_2O_3_23%C, and Fe_2O_3_36%C cells, respectively. However, in the successive cycles these values increased noticeably. The highest Coulombic efficiency after the first cycle was that of the cell containing the Fe_2O_3_23%C composite, probably in large part resulting from the homogeneous particle size distribution of the γ-Fe_2O_3.

The rate performance of cells containing Fe_2O_3_air, Fe_2O_3_23%C, and Fe_2O_3_36%C samples tested at different discharge rates ranging between C/10 and 2C is shown in Figure 14. Due to the limited diffusion of lithium ions in the cell, the three samples show decreased capacities at the higher rates. However, when reducing the discharge rate back to C/5 and C/10, both of the composites recover the capacity better. This fact could be attributed to the electric connection that the carbon matrix provides. Thus, composite materials show a promising electrochemical performance providing a specific discharge capacity of around 1200 mAh/g after operating for 100 cycles at 1C. These excellent results could be explained by considering the structural and particle size homogeneity as well as the γ-Fe_2O_3 nanoparticle uniform distribution in the *in situ* generated amorphous carbon matrix.

DOI: 10.1021/acs.inorgchem.5b00203
Inorg. Chem. 2015, 54, 5239−5248

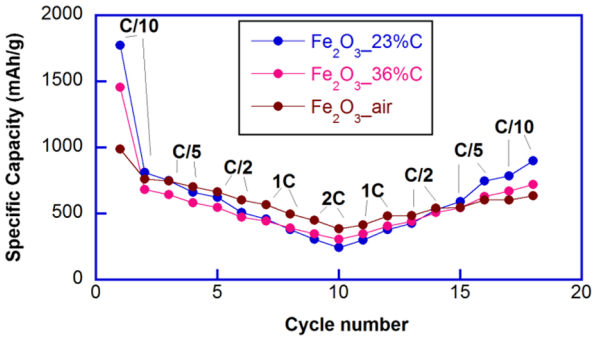

Figure 14. Rate discharge capabilities for Fe_2O_3_air, Fe_2O_3_23%C, and Fe_2O_3_36%C samples.

CONCLUSIONS

Fe_2O_3_air, Fe_2O_3_23%C, and Fe_2O_3_36%C samples were successfully prepared by a freeze-drying method. X-ray diffraction measurements showed that the Fe_2O_3_air sample crystallizes primarily as the α- Fe_2O_3 hematite structure, although some weak reflections corresponding to γ-Fe_2O_3 were also detected. In contrast, the Fe_2O_3_23%C and Fe_2O_3_36%C composites crystallize in the γ-Fe_2O_3 maghemite structure. The morphologic study revealed that Fe_2O_3_23%C and Fe_2O_3_36%C samples are more homogeneous than Fe_2O_3_air. It was also observed that the Fe_2O_3 particles are well-dispersed in the matrix of amorphous carbon that was generated *in situ* during the synthesis procedure. Electron paramagnetic resonance and Mössbauer spectroscopy corroborated that described composition and morphology. The magnetic measurements for the carbonaceous composites showed a lack of saturation of the magnetization at high magnetic fields (>20 kOe) and a narrowing of the central area of the hysteresis loop for the Fe_2O_3_36%C sample. This would be associated with the existence of very small isolated maghemite nanoparticles, which would be far away from the magnetic saturation at the experimental temperature. Moreover, magnetization versus temperature measurements for these samples showed the presence of para- and superparamagnetic contributions ascribed to very small superparamagnetic γ-Fe_2O_3 nanoparticles. The electrochemical study revealed that composite materials show a promising electrochemical performance. This could be attributed to several factors, such as the suitable morphology of the samples and the good connection that provides the *in situ* generated carbon matrix without blocking the lithium ion diffusion pathways. In this context, in order to obtain the best electrochemical performance in these materials, a precise optimization of the carbon amount should be performed.

EXPERIMENTAL SECTION

Materials and Reagents. The following materials and reagents were used as purchased without further purification: citric acid monohydrate (99.5%, Sigma-Aldrich) and iron(III) citrate (98%, Sigma-Aldrich).

Sample Preparation. Three iron oxide samples were synthesized by the freeze-drying method. For the sample designated Fe_2O_3_air only $C_6H_5FeO_7$ was dissolved in 25 mL of water. For the other two samples $C_6H_8O_7{\cdot}H_2O$ and $C_6H_5FeO_7$ reagents were added in the molar ratios of 1:2 and 2:1, in order to produce composites with different carbon contents. The resulting solutions were subsequently frozen in a round-bottom flask that contained liquid nitrogen. Afterward, the round-bottom flasks were connected to the freeze-dryer for 48 h at a pressure of 3 × 10−1 mbar and a temperature of −80 °C to sublime the solvent. The as-obtained precursors were subjected to a single heat treatment at 400 °C for 6 h. The heat treatment of the Fe_2O_3_air sample was carried out in air while the other two samples were calcined in a nitrogen atmosphere. Subsequently, the products were ball-milled for 30 min.

Characterization. A PerkinElmer 2400CHN analyzer was employed to determine the carbon content of the samples. Structural characterization of the samples was carried out using X-ray powder diffraction with a Bruker D8 Advance Vario diffractometer using Cu Kα radiation. The obtained diffractograms were profile-fitted using the FullProf program.[41] The morphologies of the materials were studied by transmission electron microscopy (TEM) using a FEI TECNAI F30 and by a scanning electron microscope (JEOL JSM 7500F). A Bruker ELEXSYS 500 spectrometer equipped with a super-high-Q resonator ER-4123-SHQ, operating at the X-band, was used to record the EPR polycrystalline spectra. Magnetic susceptibility measurements (dc) were carried out between 5 and 300 K with a Quantum Design SQUID magnetometer. Mössbauer spectroscopic studies were performed on the oxidized composite using a constant acceleration spectrometer with a 57CoRh source. Velocity calibration was carried out by using a metallic Fe foil, and the Mössbauer spectra parameters are given relative to this standard at room temperature. The spectra were fitted with the NORMOS program.[42]

There were 2032 coin cells assembled to evaluate the electrochemical performances of the samples. To prepare the electrodes, the active materials were mixed with conducting carbon black (Super P, Timcal) and polyvinylidene fluoride (PVDF) binder with weight ratios of 70:15:15 and dispersed in *N*-methyl-2-pyrrolidone (NMP) to form a slurry. The slurry was then cast onto Cu current collectors and dried at 120 °C in a vacuum oven overnight. Electrochemical cells with metallic lithium foils as counter electrodes, Celgard 2400 polypropylene separators, and 1 M $LiPF_6$ in 50%−50% ethyl carbonate (EC) and dimethyl carbonate (DMC) as the electrolytic solution were assembled in an Ar-filled glovebox. All the electrochemical measurements were carried out on a Bio-Logic VMP3 potentiostat/galvanostat at room temperature. Typical electrode loadings were 1.3 mg/cm^2.

The galvanostatic charge/discharge experiments were performed between 0.1 and 3 V at 0.1C and 1C current rates where 1C is defined as the rate at which the total theoretical capacity based on full conversion can be discharged in 1 h

$$Fe_2O_3 + 6Li + 6e - \leftrightarrow 2Fe + 3Li_2O$$

To calculate the capacity values, the weight of only the Fe_2O_3 was considered, not including the *in situ* carbon.

AUTHOR INFORMATION

Corresponding Author

*E-mail: trojo@cicenergigune.com. Phone: +34945 297 108.

Notes

The authors declare no competing financial interest.

ACKNOWLEDGMENTS

This work was financially supported by the Ministerio de Economía y Competitividad (MAT2013-41128-R and ENE2013-44330-R) and the Gobierno Vasco/Eusko Jaurlaritza (IT570-13, ETORTEK CICENERGIGUNE10, SAIOTEK S-PE12UN140). A.I. thanks the Gobierno Vasco/Eusko Jaurlaritza for a fellowship.

REFERENCES

(1) Scrosati, B. *Nature* **1995**, *373*, 557.
(2) Tarascon, J. M.; Armand, M. *Nature* **2001**, *414*, 359.
(3) Nagaura, T.; Tozawa, K. *Prog. Batteries Sol. Cells* **1990**, *9*, 209.
(4) Nishi, Y. *Chem. Rec.* **2001**, *1*, 406.
(5) Bruce, P. G.; Scrosati, B.; Tarascon, J. M. *Angew. Chem., Int. Ed.* **2008**, *47*, 2930−2946.

DOI: 10.1021/acs.inorgchem.5b00203
Inorg. Chem. 2015, 54, 5239−5248

(6) Poizot, P.; Laruelle, S.; Grugeon, S.; Dupont, L.; Tarascon, J. M. *Nature* **2000**, *407*, 496−499.
(7) Li, J.; Dahn, H. M.; Krause, L. J.; Le, D. B.; Dahn, J. R. *J. Electrochem. Soc.* **2008**, *155*, A812−A816.
(8) Hassoun, J.; Lee, K.-S.; Sun, Y.-K.; Scrosati, B. *J. Am. Chem. Soc.* **2011**, *133*, 3139−3143.
(9) Ortiz, G. F.; Tirado, J. L. *Electrochem. Commun.* **2011**, *13*, 1427−1430.
(10) Chen, J.; Xu, L. N.; Li, W. Y.; Gou, X. L. *Adv. Mater.* **2005**, *17*, 582−586.
(11) Lian, P. C.; Zhu, X. F.; Xiang, H. F.; Li, Z.; Yang, W. S.; Wang, H. H. *Electrochim. Acta* **2010**, *56*, 834−840.
(12) Shi, W.; Zhu, J. X.; Sim, D. H.; Tay, Y. Y.; Lu, Z. Y.; Zhang, X. J.; Sharma, Y.; Srinivasan, M.; Zhang, H.; Hng, H. H.; Yan, Q. Y. *J. Mater. Chem.* **2011**, *21*, 3422−3427.
(13) Ban, C. M.; Wu, Z. C.; Gillaspie, D. T.; Chen, L.; Yan, Y. F.; Blackburn, J. L.; Dillon, A. C. *Adv. Mater.* **2010**, *42*, E145−E149.
(14) Han, S. W.; Jung, D. W.; Jeong, J. H.; Oh, E. S. *J. Appl. Electrochem.* **2012**, *42*, 1057−1064.
(15) Palomares, V.; Goñi, A.; Gil de Muro, I.; de Meatza, I.; Bengoechea, M.; Miguel, O.; Rojo, T. *J. Power Sources* **2007**, *171* (2), 879−885.
(16) Palomares, V.; Goñi, A.; Gil de Muro, I.; de Meatza, I.; Bengoechea, M.; Cantero, I.; Rojo, T. *J. Electrochem. Soc.* **2009**, *156* (10), A817.
(17) Ishikawa, K.; Yoshiikawa, K.; Okada, N. *Phys. Rev. B* **1998**, *37*, 5852.
(18) Birks, L. S.; Friedman, H. *J. Appl. Phys.* **1946**, *17*, 687.
(19) Weil, J. A., Bolton, J. R., Wertz, J. E. *Electron Paramagnetic Resonance: Elementary Theory and Applications*; Wiley Interscience: New York, 1994.
(20) Johnson, H. P.; Lowrie, W.; Kent, D. V. *Geophys. J. R. Astron. Soc.* **1975**, *41*, 1−10.
(21) Ramos Guivar, J. A.; Bustamante, A.; Flores, J.; Mejía Santillán, M.; Osorio, A. M.; Martinez, A. I.; De Los Santos Valladares, L.; Barnes, C. H. W. *Hyperfine Interact.* **2014**, *224*, 89−97.
(22) Cullity, B. D. *Introduction to Magnetic Materials*; Addison-Wesley: Boston, MA, 1972.
(23) Franco, A.; Zapf, V. S.; Barbeta, V. B.; Jardim, R. F. *J. Appl. Phys.* **2010**, *107*, 073904.
(24) Roca, A. G.; Marco, J. F.; del Puerto Morales, M.; Serna, C. J. *J. Phys. Chem. C* **2007**, *111*, 18577−78584.
(25) Martinez, B.; Obradors, X.; Balcells, Ll.; Rouanet, A.; Monty, C. *Phys. Rev. Lett.* **1997**, *80*, 181−183.
(26) Zboril, R.; Mashlan, M.; Petridis, D. *Chem. Mater.* **2002**, *14*, 969−982.
(27) Da Costa, G. M.; De Grave, E.; Bowen, L. H.; Vanderberghe, R. E.; De Bakker, A. P. M. *Clays Clay Miner.* **1994**, *42*, 628−633.
(28) Roca, A. G.; Marco, J. F.; Morales, M. P.; Serna, C. J. *J. Phys. Chem. C* **2007**, *111*, 18577−18584.
(29) Neél, L. *C. R. Hebd. Seances Acad. Sci.* **1949**, *228*, 664.
(30) Wang, P.; Gao, M.; Pan, H.; Zhang, J.; Liang, C.; Wang, J.; Zhou, P. *J. Power Sources* **2013**, *239*, 466−474.
(31) Yuan, S. M.; Li, J. X.; Yang, L. T.; Su, L. W.; Liu, L.; Zhou, Z. *ACS Appl. Mater. Interfaces* **2011**, *3*, 705.
(32) Jin, S.; Deng, H.; Long, D.; Liu, X.; Zhan, L.; Liang, X.; Qiao, W.; Ling, L. *J. Power Sources* **2011**, *196*, 3887.
(33) López, M. C.; Ortiz, G. F.; Lavela, P.; Alcántara, R.; Tirado, J. L. *ACS Sustainable Chem. Eng.* **2013**, *1*, 46−56.
(34) Lindström, H.; Södergren, S.; Solbrand, A.; Rensmo, H.; Hjelm, J.; Hagfeldt, A.; Lindquist, S.-E. *J. Phys. Chem. B* **1997**, *101*, 7717−7722.
(35) Conway, B. E.; Birss, V.; Wojtowicz, J. *J. Power Sources* **1997**, *66*, 1−14.
(36) Zhou, G.; Wang, D.-W.; Li, F.; Zhang, L.; Li, N.; Wen L, W Z-S.; Lu, G. Q.; Chen, H.-M. *Chem. Mater.* **2010**, *22*, 5306−5313.
(37) Gónzalez, J. R.; Menéndez, R.; Álcantara, R.; Nacimiento, F.; Tirado, J. L.; Zhecheva, E.; Stoyanova, R. *Ultrason. Sonochem.* **2015**, *24*, 238.
(38) Debart, A.; Dupont, L.; Poizot, O.; Leriche, J. B.; Tarascon, J. M. *J. Electrochem. Soc.* **2001**, *148*, A1266.
(39) Laruelle, S.; Grugeon, S.; Poizot, P.; Dolle, M.; Dupont, L.; Tarascon, J. M. *J. Electrochem. Soc.* **2002**, *149*, A627.
(40) Jiao, F.; Bao, J.; Bruce, P. G. *Electrochem. Solid-State Lett.* **2007**, *10*, A264−A266.
(41) Rodríguez-Carvajal J. http://valmap.dfis.ull.es/fullprof/index.php.
(42) Brand, A.; Lauer, I.; Herkach, D. M. *J. Phys. (Paris)* **1983**, *F13*, 675.

DOI: 10.1021/acs.inorgchem.5b00203
Inorg. Chem. 2015, 54, 5239−5248